Mesoscale Effects in Electrochemical Conversion: Coupling of Chemistry to Atomic- and Nanoscale Structure in Iron-Based Electrodes

Kamila M. Wiaderek,[†] Olaf J. Borkiewicz,[†] Nathalie Pereira,[‡] Jan Ilavsky,[†] Glenn G. Amatucci,[‡] Peter J. Chupas,[†] and Karena W. Chapman*,[†]

[†]X-ray Science Division, Advanced Photon Source, Argonne National Laboratory, Argonne, Illinois 60439, United States
[‡]Department of Materials Science and Engineering, Rutgers University, North Brunswick, New Jersey 08902, United States

S *Supporting Information*

ABSTRACT: The complex coupling of atomic, chemical, and electronic transformations across multiple length scales underlies the performance of electrochemical energy storage devices. Here, the coupling of chemistry with atomic- and nanoscale structure in iron conversion electrodes is resolved by combining pair distribution function (PDF) and small-angle X-ray scattering (SAXS) analysis for a series of Fe fluorides, oxyfluorides, and oxides. The data show that the anion chemistry of the initial electrode influences the abundance of atomic defects in the Fe atomic lattice. This, in turn, is linked to different atom mobilities and propensity for particle growth. Competitive nanoparticle growth in mixed anion systems contributes to a distinct nanostructure, without the interconnected metallic nanoparticles formed for single anion systems.

Batteries are complex multicomponent devices wherein mesoscale phenomena—the nanoscale structure and chemistry of different components, and interactions thereof—drive functionality and performance.[1−4] For example, nanostructuring of the composite electrodes provides bicontinuous electrically and ionicaly conductive paths essential to electron/ion transport, while excessive nanoparticle growth and phase segregation can reduce reversibility.[5,6] For conversion-based electrodes, where large-scale structural and chemical transformations occur, understanding and controlling the nanostructure is critical to optimizing performance. While conversion can provide higher energy storage capacities than conventional electrodes, based on Li-insertion, limited cycling rates and reversibility impede progress toward real-world applications.[7−9] The higher capacity of such conversion reactions stems from the multiple electron transfer per metal center; upon lithiation, the transition metal is fully reduced to the zerovalent M^0 state. In contrast to intercalation, where the atomic structure of the electrode is only slightly perturbed by Li-insertion, during conversion, the electrode structure and chemistry transforms completely, producing multiple phases according to the general mechanism $M^{y+} X^{z-}_{y/z} + yLi^0 + ye^- \rightarrow M^0 + {}^y/_z Li_z X$ (where X = O^{2-}, F^-, etc.).

Electrochemical conversion of different salts of a given metal yields a common and ostensibly identical product: the zerovalent metal. For example, maximal lithiation of iron-based electrodes (to ca. 0 V) produces metallic iron nanoparticles for oxide, fluoride, and oxyfluoride electrodes alike.[8−10] Accordingly, these provide an opportunity to explore the coupling of nanostructure development and anion chemistry, and correlate these with electrochemical performance.

Here we combine synchrotron-based small-angle X-ray scattering (SAXS) and pair distribution function (PDF) measurements to probe metallic iron formed by electrochemical conversion of different iron compounds (Fe_2O_3, FeO, FeF_2, FeF_3, and $Fe^{II}_{(1-x)}Fe^{III}_xO_xF_{(2-x)}$, x = 0.5, 0.6) and evaluate the influence of anion chemistry and reaction temperature on the atomic- and nanoscale structure. The PDF probes the local atomic structure of the Fe particles to identify deviations from the average body-centered cubic (bcc) structure. SAXS analysis of the same samples reveals the nanostructure formed by the Fe particles. We find that the concentration of atomic defects, the particle size, shape, and particle−particle interactions are correlated to the anion chemistry of the initial electrode. The particle−particle interactions, defect chemistry and implied atomic mobility may affect the overall electrode performance and reaction kinetics.

Iron-based battery electrodes are attractive due to the high elemental abundance, low cost, and multiple accessible oxidation states. Conversion of these electrodes provides higher energy storage capacity than intercalation (>700 mA·h g^{-1} cf. ~175 mA·h g^{-1} for LiFePO$_4$).[11] While capacity retention is generally lower than for intercalation compounds, there is wide variability in the long term stability for iron-based conversion electrodes with different chemistries. The mixed-anion oxyfluoride provides the best compromise between reaction potential, rate capability and reversibility, with the best long-term cycling performance. The pure fluorides have high reaction potential but lower rate capability, while the pure oxides have lower reaction potential. For these systems, the phase evolution during conversion has been established in earlier studies based on PDF and other analyses.[5b,12−15] Generally, above an average Fe oxidation state of 2, Li insertion occurs. Beyond this, a multiphase conversion occurs whereby metallic Fe nanoparticles are extruded.

Nanocomposite electrodes of iron fluorides (FeF_2, FeF_3), oxyfluorides ($Fe^{II}_{(1-x)}Fe^{III}_xO_xF_{(2-x)}$, $x = 0.5–0.6$),[10] and iron oxides (Fe_2O_3, FeO) containing 60 wt % of active material and 40 wt % of graphite, Vulcan C and PTFE (1:1:2) were prepared as described previously.[16] These were lithiated at constant current (50 μA g^{1-}) to 0.2 V at 25 and 60 °C, recovered in an Ar-atmosphere, and sealed in a glass capillary for X-ray measurements.

SAXS data were collected at beamline 12-ID-B, at the Advanced Photon Source, at Argonne National Laboratory, using a PILATUS 2M detector (Dectris Ltd.) enclosed within a vacuum chamber (~12 keV; λ = 1.033 Å). The detector, positioned 2 m from the sample, measured scattering in the Q-range 0.007−0.66 Å^{-1}. SAXS data were analyzed using the *Modeling II* tool of the Irena package within IGOR Pro.[17] Size distribution of spherical particles with assumption of interference structure factor when needed was applied.[18] Gaussian and log-normal size distributions were evaluated.

Total scattering data suitable for PDF analysis were collected at beamline 11-ID-B. High energy X-rays (58.26 keV, λ = 0.2128 Å) were combined with a large amorphous silicon-based area detector (Perkin-Elmer) to collect data to high Q-values (Q_{max} = 24 Å^{-1}).[19] The images were reduced to one-dimensional data with fit2d.[20] The data were corrected for background, Compton scattering, and detector geometry and Fourier transformed to yield the PDF, $G(r)$, within PDFgetX2.[21] Structural models were refined against the PDF data within PDFgui.[22] The relative intensities and position of peaks in the PDF that define the local atomic structure were quantified by fitting Gaussian functions within fityk.[23]

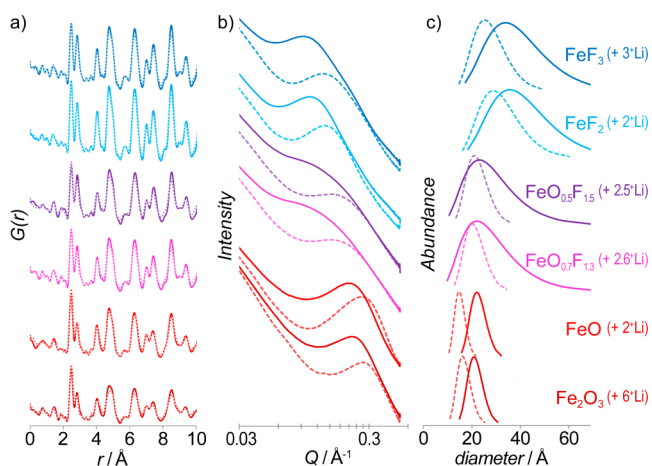The SAXS and PDF data, shown in Figure 1, reveal variability in the local atomic structure and the Fe

Figure 1. The PDFs (a), SAXS data (b), and the corresponding (log-normal) particle size distributions (c) for Fe^0 nanoparticles formed through electrochemical conversion of a series of Fe electrodes at 25 and 60 °C (dashed and continuous lines, respectively).

nanostructure with reaction temperature and anion chemistry of the precursor. The PDFs for the lithiated electrodes are dominated by correlations from bcc Fe. The corresponding background-corrected SAXS data shows features in the Q-range 0.09−0.30 Å^{-1}, arising from nanoparticles of 2−4 nm size.

Atomic structure models for bcc Fe were refined against the PDF data (r-range, 1−30 Å) to evaluate the lattice dimensions and the coherence length (here the nanoparticle size, see Supporting Information). The most pronounced deviations in

the fits to the data occur at low r, reflecting local defects in the average bcc structure that perturb the first and second nearest neighbor distances (at 2.5 and 2.8 Å). The defects were more apparent at 25 °C compared to 60 °C. The local defects in the bcc atomic structure were characterized by reduced intensity (i.e., coordination number) and distance for the second nearest-neighbor Fe···Fe distance (along the unit cell edge) compared to bulk Fe metal (Figure 2).
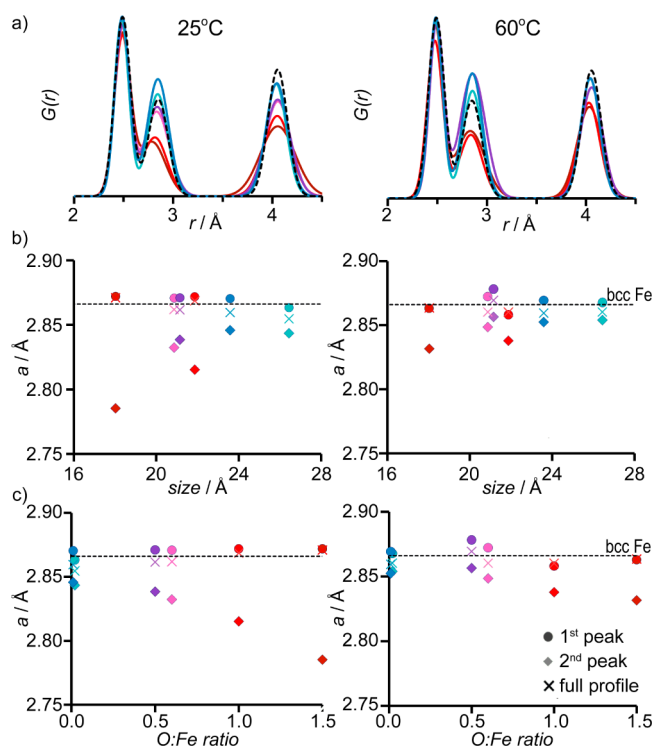

Figure 2. (a) Gaussian functions fit to the shortest Fe···Fe distances for ideal bcc Fe^0 (dashed) and Fe^0-derived from conversion reactions at 25 and 60 °C. The lattice parameter (a) implied by the 2nd Fe−Fe distance (at ~2.8 Å) provides a measure of defect concentration, deviating from that implied by the 1st Fe···Fe distance (~2.5 Å), and the obtained full profile (1−30 Å) fits to the PDFs and an ideal bcc structure. Correlation of the defect concentration (i.e., 2nd neighbor implied lattice parameter) with the refined particle size (b) and O:Fe ratio (c) shows that the anion chemistry is most directly linked the defect concentration.

An estimate of the defect concentration, based on degree of deviation of the second nearest-neighbor Fe−Fe distance from a regular bcc structure, was used to identify possible correlations with the Fe nanoparticle size and system chemistry. While defect concentration and strain are often linked to particle size,[24] here, these are only loosely correlated ($R^2 = 0.60$ at 25 °C, see Figure 2b). Instead, the defect level, at 25 °C, is strongly correlated with the composition of the precursor electrode increasing linearly ($R^2 = 0.95$) with the oxygen content (i.e., the O:Fe ratio, see Figure 2c). We postulate that at higher temperature, an accelerated restructuring or annealing contributes to the reduced level of defects observed.

The forms of the SAXS profiles are indicative of spheroidal scatterers in densely packed arrangements, and not rods or discs. Well-defined particle−particle interactions are suggested by inversions in the gradient with increasing Q (i.e., the U-shaped feature in the SAXS profile, see Figure 1b). This "structural" contribution complicates the quantitative SAXS

analysis; the nanostructure (number and distance of neighboring particles) must be accurately modeled to determine the primary nanoparticle size. Here, the data were modeled as monomodal distributions of spheroidal scatterers (i.e., the Fe nanoparticles), with an interference structure factor, based on a hard-sphere model, used to account for the nanoparticle interactions.

Larger nanoparticles with broader size distributions were generally observed for Fe^0 derived from fluoride-rich compared to oxygen-rich precursor electrodes (Figures 1c and 2). For conversion at high temperature, the SAXS features were observed at lower Q-values, corresponding to larger nanoparticles (by ca. 25%). With exception of FeO_xF_{2-x} electrodes lithiated at high temperature, the dominant nanoparticle diameter (mode) from both log-normal and Gaussian distributions were in close agreement (<0.5 Å, see Supporting Information).

The primary Fe nanoparticles were well modeled by a perfect spherical geometry, with no significant elongation or compression (i.e., prolate or oblate spheroids) except in the case of FeO_xF_{2-x} electrodes lithiated at high temperature. Each spherical Fe nanoparticle, in a single anion system, was surrounded by an average 3–4 neighboring nanoparticles (Figure 3), with little (<10%) temperature-dependence. The nanoparticles were separated by 1–9 Å, with the largest separation observed for FeF_3-derived Fe.
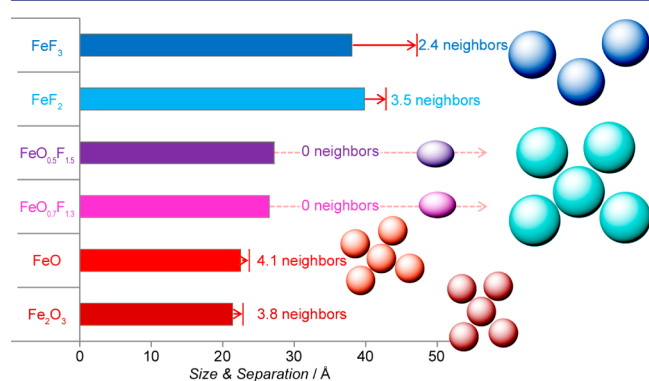

Figure 3. The Fe^0 nanostructure resulting from lithiation of different Fe electrodes at 60 °C. The dominant (mode) primary particle size (bars), the average particle–particle separation (arrows), and number of well-defined neighboring particles are indicated.

Conversion of FeO_xF_{2-x} produced unusual Fe nanostructures compared to those derived from pure oxide and fluoride precursor electrodes, with few (<1.5) well-defined neighbors for reaction at room temperature, and no well-defined neighbors for reaction at high temperature (Figure 3). Increased polydispersity at high temperature may reflect a significantly larger particle size distribution or distortion of the Fe nanoparticles as prolate spheroids elongated by ca. 40–60%.

For the series of electrodes, the atomic defect concentration, particle size and size distribution of the Fe nanoparticles formed during conversion varies significantly with the initial anion chemistry. The abundance of local atom defects is positively correlated with the initial O content, while the Fe nanoparticle size and size distribution increase with F content. Given the correlation of defects with O, we propose that the local structural distortions are associated with O species which may either contribute to defect formation or may inhibit annealing of naturally formed defects. This may be a

consequence of the strong affinity of oxygen toward Fe which likely reduces Fe mobility. The local structure of the atomic defects, with contraction and reduced intensity of the second Fe⋯Fe peak, is consistent with the presence of vacancies or substitutional defects (possibly O) within the bcc lattice.

From comparison of reactions at different temperature, higher temperature Fe conversion results in a larger average particle size, a broader size distribution and reduced defect concentration. The elevated temperatures, which enhance atom mobility and reaction kinetics, can be seen as representing a more advanced or well equilibrated reaction state. The reduced defect concentration at higher temperature suggests progressive defect annealing which is accelerated with temperature. Atomic structural defects, such as these, have been previously observed for α-Fe_2O_3 in a systematic study as a function of lithiation.[13] In that system, the decrease in defect concentration as the lithiation reaction progressed also suggests that the defect Fe structure is not the thermodynamic minimum and that the defects heal as the system approaches equilibrium, an observation that is consistent with the differences found here at higher temperatures.

The trends observed in nanoparticle size and size distributions can be linked to the defect concentration and, in turn, to the anion chemistry of the initial electrode. This can again be understood considering how defect structure and nanoparticle size evolve during conversion of α-Fe_2O_3.[13] There, restructuring of the nanoparticle defects occurred at the expense of nanoparticle growth. This suggests that the thermodynamic energy penalty associated with the defects is greater than that associated with the surface energy (though in this composite system, the surface may be passivated or stabilized). Here, restructuring of defect-rich (i.e., O-rich) systems instead of particle growth can be linked to the smaller nanoparticle sizes found for more O-rich systems. By contrast, enhanced atomic mobility is evident in defect-free, F-rich systems where larger particle sizes are evident.

The type of nanostructure formed in electrodes with a single anion (i.e., the pure fluorides or oxides) is remarkably consistent—an interconnected network with each primary particle having between 3 and 4 neighbors—and independent of the size or size distribution of the primary particle. The nanostructures formed for the mixed-anion FeO_xF_{2-x} phases are different in that there are no (or very few) well-defined neighboring particles and, hence, no interconnected network of particles.[25] We postulate that the contrasting nanostructures, observed for single- and mixed-anion systems, may reflect differences in the properties of particles nucleated in O- or F-rich environments. The more defect-rich particles nucleated in more O-rich environments may have enhanced atomic mobility and persistence than the less defect-rich particles nucleated in more F-rich environments. In single-anion electrodes, nuclei form in a uniform anion environment, with the same level of defects and growth potential. However, in the mixed-anion systems, defect-rich and defect-poor particles may nucleate in the locally heterogeneous anion-environments (either O-rich or F-rich). The defect-rich particles will be more persistent, while the lower defect particles with more mobile Fe atoms may be eliminated through redistribution of atoms to the other, more persistent nuclei, thereby leading to a lower density packing of particles and fewer particle–particle interactions.

While an interconnected network of metallic nanoparticles may allow for electrical conduction paths for some electrodes, clearly this is not the case in FeO_xF_{2-x}. The exemplary

electrochemical performance of these systems suggests a different, but equally effective, electrical conductive path must exist within the potential window that provides optimal cycling performance and capacity retention (4.5−1.5 V),[8] perhaps associated with one of the lithiated intermediate phases.

In summary, probing the atomic and nanoscale structure in Fe formed through electrochemical conversion in different anion environments and at different temperatures has provided insight into the mesoscale phenomena. By combining PDF and SAXS, we can understand the link between chemistry and structure across multiple length scales. The nanostructure insights provided here by SAXS methods are comparable to widely used electron microscopies, although with several distinct advantages: it is more intrinsically quantitative; as a bulk probe it avoids sampling biases; and it avoids artifacts associated with sample damage in the electron beam. Applied in situ, it provides more representative insights than TEM where the in situ measurements under relevant electrochemical cycling conditions remains an outstanding challenge. The anion chemistry of the initial electrode governs the Fe particle size and nanostructure by influencing defect formation, annealing, atomic mobility, and particle growth rates. In a fluorine-rich environment, Fe atoms have enhanced mobility, leading to more facile annealing and particle growth. In an oxygen-rich environment, more defects are formed and defect annealing dominates growth. The formation of unusual nanostructures in the mixed anion phases, without an interconnected network of Fe nanoparticles, may be attributed to the competitive growth of Fe nanoparticles nucleated in different anion environments, with different defect concentrations.

■ ASSOCIATED CONTENT

ⓢ Supporting Information

Details of sample preparation, electrochemistry and PDF and SAXS modeling. This material is available free of charge via the Internet at http://pubs.acs.org.

■ AUTHOR INFORMATION

Corresponding Author

chapmank@aps.anl.gov

Notes

The authors declare no competing financial interest.

■ ACKNOWLEDGMENTS

■ REFERENCES

(1) (a) Hemminger, J. *From Quanta to the Continuum: Opportunities for Mesoscale Science*; Department of Energy: Washington, DC, 2012;. (b) Crabtree, G. W.; Sarrao, J. L. *MRS Bull.* **2012**, *37*, 1079.

(2) (a) Zhang, Q.; Uchaker, E.; Candelariaz, S. L.; Cao, G. *Chem. Soc. Rev.* **2013**, *42*, 3127. (b) Wagemaker, M.; Mulder, F. M. *Acc. Chem. Res.* **2013**, *46*, 1206.

(3) (a) Pereira, N.; Klein, L. C.; Amatucci, G. G. *Solid State Ionics* **2004**, *167*, 29. (b) Guo, Y. G.; Hu, Y. S.; Sigle, W.; Maier, J. *Adv. Mater.* **2007**, *19*, 2087.

(4) (a) Boesenberg, U.; Meirer, F.; Liu, Y. J.; Shukla, A. K.; Dell'Anna, R.; Tyliszczak, T.; Chen, G. Y.; Andrews, J. C.; Richardson, T. J.; Kostecki, R.; Cabana, J. *Chem. Mater.* **2013**, *25*, 1664. (b) Liu, X. S.; Wang, D. D.; Liu, G.; Srinivasan, V.; Liu, Z.; Hussain, Z.; Yang, W. L. *Nat. Commun.* **2013**, *4*, 2568. (c) Robert, D.; Douillard, T.; Boulineau, A.; Brunetti, G.; Nowakowski, P.; Venet, D.; Bayle-Guillemaud, P.; Cayron, C. *ACS Nano* **2013**, *7*, 10887.

(5) (a) Wang, F.; Yu, H. C.; Chen, M. H.; Wu, L. J.; Pereira, N.; Thornton, K.; Van der Ven, A.; Zhu, Y. M.; Amatucci, G. G.; Graetz, J. *Nat. Commun.* **2012**, *3*, 1201. (b) Wang, F.; Robert, R.; Chernova, N. A.; Pereira, N.; Omenya, F.; Badway, F.; Hua, X.; Ruotolo, M.; Zhang, R.; Wu, L.; Volkov, V.; Su, D.; Key, B.; Whittingham, M. S.; Grey, C. P.; Amatucci, G. G.; Zhu, Y.; Graetz, J. *J. Am. Chem. Soc.* **2011**, *133*, 18828.

(6) Harris, S. J.; Lu, P. *J. Phys. Chem. C* **2013**, *117*, 6481.

(7) Poizot, P.; Laruelle, S.; Grugeon, S.; Dupont, L.; Tarascon, J. M. *Nature* **2000**, *407*, 496.

(8) (a) Badway, F.; Pereira, N.; Cosandey, F.; Amatucci, G. G. *J. Electrochem. Soc.* **2003**, *150*, A1209. (b) Badway, F.; Cosandey, F.; Pereira, N.; Amatucci, G. G. *J. Electrochem. Soc.* **2003**, *150*, A1318.

(9) Amatucci, G. G.; Pereira, N. *J. Fluorine Chem.* **2007**, *128*, 243.

(10) Pereira, N.; Badway, F.; Wartelsky, M.; Gunn, S.; Amatucci, G. G. *J. Electrochem. Soc.* **2009**, *156*, A407.

(11) Cabana, J.; Monconduit, L.; Larcher, D.; Palacin, M. R. *Adv. Mater.* **2010**, *22*, E170.

(12) Yamakawa, N.; Jiang, M.; Key, B.; Grey, C. P. *J. Am. Chem. Soc.* **2009**, *131*, 10525.

(13) Shyam, B.; Chapman, K. W.; Balasubramanian, M.; Klingler, R. J.; Srajer, G.; Chupas, P. J. *Angew. Chem., Int. Ed.* **2012**, *51*, 4852.

(14) Wiaderek, K. M.; Borkiewicz, O. J.; Castillo-Martínez, E.; Robert, R.; Pereira, N.; Amatucci, G. G.; Grey, C. P.; Chupas, P. J.; Chapman, K. W. *J. Am. Chem. Soc.* **2013**, *135*, 4070.

(15) Sina, M.; Nam, K.-W.; Su, D.; Pereira, N.; Yang, X.-Q.; Amatucci, G. G.; Cosandey, F. *J. Mater. Chem. A* **2013**, *1*, 11629.

(16) Borkiewicz, O. J.; Shyam, B.; Wiaderek, K. M.; Kurtz, C.; Chupas, P. J.; Chapman, K. W. *J. Appl. Crystallogr.* **2012**, *45*, 1261.

(17) Ilavsky, J.; Jemian, P. R. *J. Appl. Crystallogr.* **2009**, *42*, 347.

(18) Beaucage, G. In *Polymer Science: A Comprehensive Reference*; Matyjaszewski, K., Möller, M., Eds.; Elsevier: Amsterdam, 2012, 399.

(19) (a) Chupas, P. J.; Qiu, X.; Hanson, J. C.; Lee, P. L.; Grey, C. P.; Billinge, S. J. L. *J. Appl. Crystallogr.* **2003**, *36*, 1342. (b) Chupas, P. J.; Chapman, K. W.; Lee, P. L. *J. Appl. Crystallogr.* **2007**, *40*, 463.

(20) Hammersley, A. P.; Svensson, S. O.; Hanfland, M.; Fitch, A. N.; Häusermann, D. *High Pressure Res.* **1996**, *14*, 235.

(21) Qiu, X.; Thompson, W.; Billinge, S. J. L. *J. Appl. Crystallogr.* **2004**, *37*, 678.

(22) Farrow, C. L.; Juhás, P.; Liu, J. W.; Bryndin, D.; Božin, E. S.; Bloch, J.; Proffen, T.; Billinge, S. J. L. *J. Phys.: Condens. Matter* **2007**, *19*, 335219.

(23) Wojdyr, M. *J. Appl. Crystallogr.* **2010**, *43*, 1126.

(24) Masadeh, A. S.; Božin, E. S.; Farrow, C. L.; Paglia, G.; Juhas, P.; Billinge, S. J. L. *Phys. Rev. B* **2007**, *76*, 115413.

(25) An interconnected network requires each particle to be surrounded by an average of 2 or more neighboring particles.